High Information Rate of 128-GBaud 1.8-Tb/s and 64-GBaud 1.03-Tb/s Signal Generation and Detection Using Frequency-Domain 8×2 MIMO Equalization

M. Nakamura, T. Kobayashi, F. Hamaoka, and Y. Miyamoto
NTT Network Innovation Laboratories, NTT Corporation, 1-1 Hikari-no-oka, Yokosuka, Kanagawa, 239–0847 Japan
masanori.nakamura.cu@hco.ntt.co.jp

Abstract: We demonstrate 1-Tb/s and 1.8-Tb/s net rate signals with 16- and 14-bit/4Dsymbol information rates at 64 and 128 GBaud by precisely equalizing transmitter- and receiver-side imperfections with frequency-domain 8×2 MIMO linear equalization and nonlinear pre-distortion.

1. Introduction

Expanding the transmission capacity of a digital-coherent transceiver is necessary to cost-efficiently accommodate continuous-growth network traffic. Transceivers capable of >1-Tb/s/wavelength operation have been intensively studied, as shown in Fig. 1 [1–13], and performance improvement of both optical frontend devices and digital signal processing has led to the achievement of >1-Tb/s capacity with the use of a flexible combination of symbol rate and information rate in accordance with various applications. In these previous studies, the signal has been generated using a high-speed complementary metal-oxide semiconductor (CMOS) digital-to-analogue converter (DAC) [1–3], Silicon-Germanium (SiGe) DAC [4–8], external electrical multiplexing DAC (MUX DAC) [9–13], or wideband optical frontend devices [12–13].

In order to further increase the information rate for >1-Tb/s/wavelength transceivers, the signal quality has to be improved by precisely compensating for the linear and nonlinear impairment of the transceivers without increasing the peak-to-average ratio (PAPR) caused by pre-distortion at the transmitter side. The PAPR increase caused by transmitter-side digital signal processing (DSP) such as spectral shaping or digital pre-distortion degrades the electrical signal-to-noise ratio (SNR). A high-quality one-sample-per-symbol signal with low PAPR can be generated by a SiGe DAC with a large analog bandwidth [6]. In the case of a one-sample-per-symbol signal without a transmitter-side DSP, the transceiver imperfection must be compensated for by the receiver-side DSP only. The time-domain complex-valued 8×2 multi-input and multi-output (MIMO) adaptive equalizer proposed in [11] can simultaneously compensate for the linear imperfections of both the transmitter and the receiver at the receiver-side DSP. However, since precise compensation for the imperfections by the 8×2 equalizer requires a large number of taps, the computational complexity exponentially increases in the time-domain convolutions.

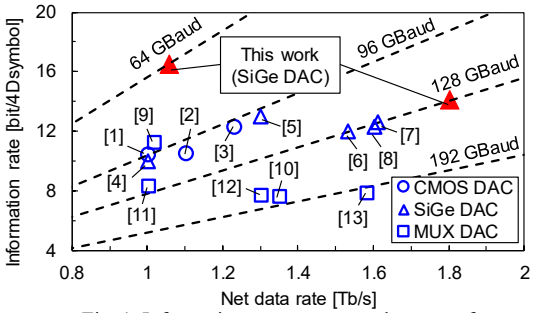

Fig. 1. Information rate versus net data rate of recent >1-Tb/s/wavelength experiments.

In this paper, we propose a low-complexity frequency-domain 8×2 MIMO adaptive equalization for precise compensation of transceiver linear impairments by efficiently calculating a large number of taps based on fast Fourier transformation (FFT). To further improve the signal quality, the nonlinear response in the modulator-driver is compensated by transmitter-side nonlinear compensation (TxNLC) with a Volterra filter [14]. The TxNLC compensates only for the nonlinearity that cannot be equalized by the linear 8×2 MIMO equalization to prevent from PAPR increasing. We experimentally demonstrate 1-Tb/s and 1.8-Tb/s net rate signals with 16- and 14-bit/4Dsymbol information rates at 64 and 128 GBaud by using a high-speed SiGe DAC and the proposed equalization.

2. Frequency-domain 8×2 MIMO adaptive equalizer

The time-domain complex-valued 8×2 MIMO adaptive equalizer enables simultaneous compensation for linear imperfections of the transmitter and receiver at the receiver-side DSP [11]. However, the time-domain convolutions in the 8×2 equalizer increase the computational complexity due to the large number of taps required for precise compensation. Frequency-domain (FD) processing [15] can significantly reduce the computational complexity since the time-domain convolutions are transformed into frequency-domain multiplications by using FFT. Therefore, we

apply FD processing to the 8×2 MIMO adaptive equalization, as shown in the block diagram of Fig. 2(a). The number of real multiplications as it relates to the computational complexity is also shown in Fig. 2(b) as a function of the number of taps. Note that in the case of the FD 8×2 MIMO, the number of taps means N/2-point FFT at the condition of 50% overlap cut. This FD 8×2 MIMO for precise compensation of the Tx- and Rx-imperfections can dramatically reduce the number of complex multiplications compared to the conventional time-domain (TD) 8×2 MIMO.

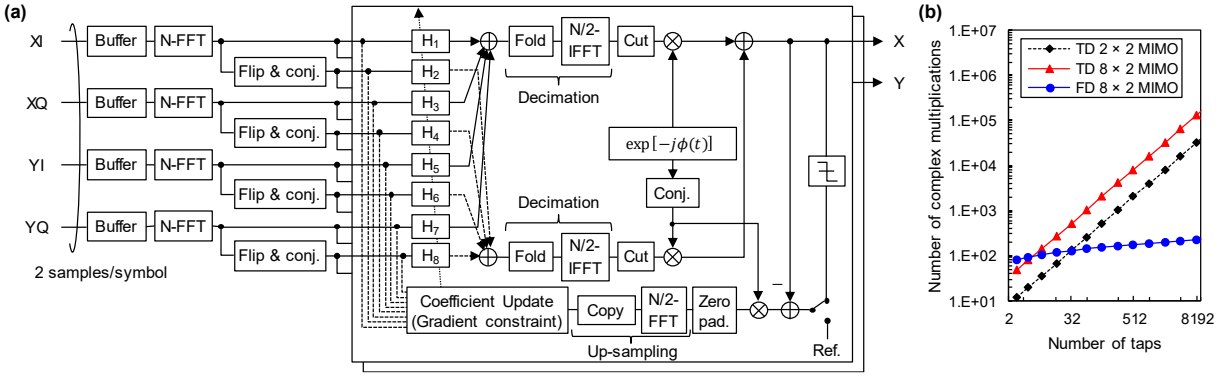

Fig. 2. (a) Block diagram of FD 8×2 MIMO adaptive equalizer and (b) computational complexity as a function of the number of taps.

3. Experimental setup

Figure 3(a) shows the experimental setup for investigating the information rate of 128- and 64-GBaud signals. The 3-dB bandwidth (BW) for each device is also shown. On the Tx side, radio frequency (RF) signals were generated by using a SiGe-DAC-based arbitrary waveform generator (AWG) operating at 128 GSa/s. Single-ended linear driver amplifiers with a gain of 11 dB were used to drive the RF signals for the lithium-niobate-based polarization-division-multiplexed in-phase-and-quadrature modulator (PDM-IQM). The PDM-QAM signal was modulated with a carrier signal of 194 THz output from an integrable tunable laser assembly (ITLA) amplified up to 25.5 dBm by using an erbium-doped fiber amplifier (EDFA). Optical equalization (OEQ) was carried out for the modulated optical signals with 64 and 128 GBaud (see Fig 3(b) and (c)). At the Rx side, the received signal was amplified using an EDFA and filtered by an optical bandpass filter (OBPF). The signals were detected by a coherent receiver composed of an optical hybrid and four balanced photo detectors (BPDs). A 256-GSa/s digital storage oscilloscope (DSO) digitized the received signal.

The functions of the offline Tx- and Rx-DSP are shown in Fig. 3(a). At the Tx-DSP, output transmitted symbols with the length of $\sim 5 \times 10^5$ were generated based on a Mersenne Twister pseudo-random number generator. The symbol sequence was up-sampled by duplicating each symbol only when the symbol rate was 64 GBaud. A Tx-side nonlinearity compensation (TxNLC) was carried out using a third-order Volterra filter with memories of $m_1 = 21, m_2 = 15,$ and $m_3 = 9$ [14]. The coefficients of the filter were determined from transmitted symbols and received symbols after carrier phase recovery (CPR). Note that we used different symbol sequences for measuring the signal quality and for training the TxNLC coefficients to avoid overfitting. The TxNLC compensates only for the nonlinearity that cannot be equalized by the 8×2 MIMO equalization to prevent PAPR from increasing. At the Rx-DSP, the sampling rate of the signal was converted into two samples per symbol. Then, compensation for the linear responses in the Tx and Rx, frequency offset compensation, and coarse CPR were simultaneously carried out using a 50% overlap cut FD 8×2 MIMO adaptive equalizer (AEQ) utilizing a pilot-assisted digital phase-locked loop with a pilot overhead (OH) of 1.59%. We used an FD-normalized least mean square algorithm [15] for the FD-AEQ-coefficient

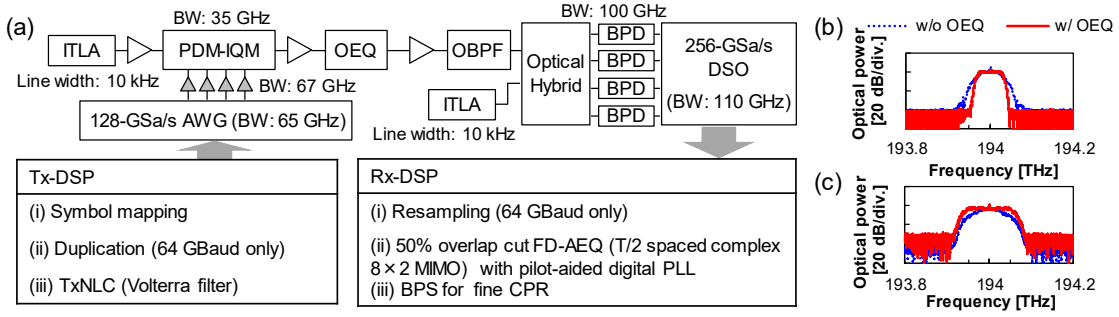

Fig. 3. (a) Experimental setup and optical spectra of (b) 64- and (c) 128-GBaud signals with and without OEQ.

update. Residual phase noise was then compensated for by a blind phase search (BPS) [16]. Finally, we evaluated the SNR and normalized generalized mutual information (NGMI) [17].

4. Results and discussion

We first evaluated the SNR of the 128-GBaud 256QAM signal. Figure 4(a) shows the FD 8×2 AEQ FFT block size dependence on the SNR at the AWG output of 480 mVpp. A >2-dB SNR improvement was observed by the proposed FD 8×2 AEQ with a sufficient FFT-block size >2048. Figure 4(b) shows the optical SNR (OSNR) versus AWG output with and without the TxNLC. The OSNRs with the TxNLC barely decreased compared to those without the TxNLC because the TxNLC only compensated for the nonlinear distortion that cannot be equalized by the linear equalizer, i.e., the FD 8×2 AEQ. Dependencies of the SNR on the OSNR are shown in Fig. 4(c) with the FD-AEQ FFT block size of 4,096. The peak SNR was improved by the TxNLC due to compensating for the saturation characteristics caused by the driver amplifiers.

Next, we used PCS signals generated by a probabilistic amplitude shaping scheme [18] to evaluate the information rate of 128- and 64-GBaud signals in the peak SNR. Figure 4(c) shows the dependences of the information rate on the NGMI for the 128-GBaud PCS-484QAM and 64-GBaud PCS-1024QAM signals. We set various information rates by changing the entropy of the distribution for the constellation points based on the Maxwell-Boltzmann distribution [18]. The measured NGMI with all information rates exceeded the NGMI limit [16]. By maximizing the transceiver performance as discussed above, the net data rates of 1.80-Tb/s 128-GBaud PCS-484QAM and 1.03-Tb/s 64-GBaud PCS-1024QAM signals were successfully achieved from {17.77 – 20×(1-0.826)}/1.0159×0.128 and {19.98 – 20×(1-0.826)}/1.0159×0.64, respectively, at the highest information rate with a pilot-OH of 1.59% and a code rate of 0.826 [16]. Finally, we transmitted the single-carrier 1.8-Tb/s 128-GBaud PCS-484QAM signal over a 30-km pure-silica-core fiber with EDFA, as shown in Fig. 4(e).

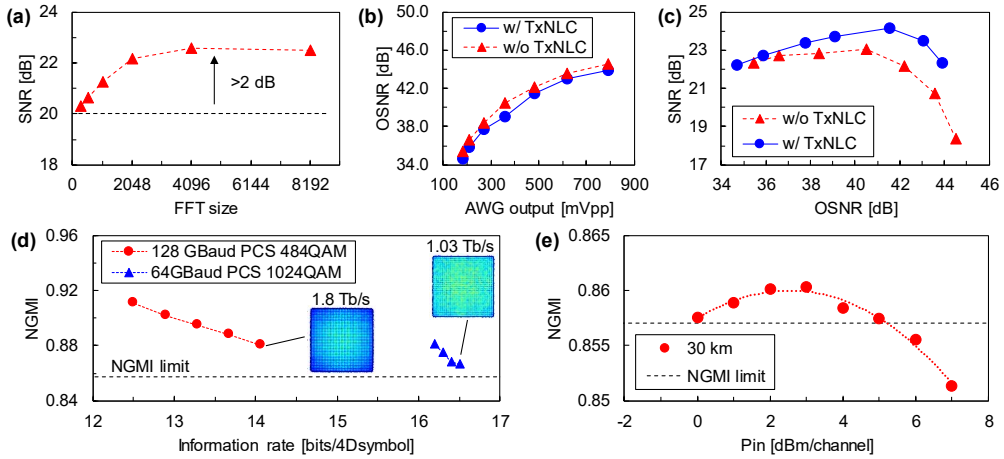

Fig. 4. Experimental results of (a) SNR v.s. FFT size of 8×2 MIMO equalizer, (b) OSNR v.s. peak-to-peak voltage of AWG output, and (c) SNR v.s. OSNR with/without TxNLC, and NGMI v.s. (d) information rate and (e) optical launched power of 1.8-Tb/s 128-GBaud signal.

5. Conclusion

We have demonstrated net rates of 1.80-Tb/s 128-GBaud PCS-484QAM and 1.03-Tb/s 64-GBaud PCS-1024QAM by precisely equalizing the Tx- and Rx-imperfections with frequency-domain 8×2 linear adaptive equalization and nonlinear compensation with a Volterra filter. The high information rates of 16-bit/4Dsymbol at 64 GBaud and 14-bit/4Dsymbol at 128 GBaud were achieved for a >1-Tb/s/wavelength high-speed transceiver.

References

[1] A. Matsushita, et al., J. Lightwave Technol. 38(11), 2905-2911 (2020).
[2] F. Buchali, et al., in Proc. OFC2020, Th3E.2 (2020).
[3] D. Che, et al, in Proc. OFC 2021, M3H.5 (2021).
[4] K. Schuh, et al., in Proc. OFC2017, Th5B.5 (2017).
[5] F. Buchali, et al., in Proc. ECOC2019, PDP.1.3 (2019).
[6] F. Buchali, et al., J. Lightwave Technol. 39(3), 763-770 (2021).
[7] V. Bajaj, et al., in Proc. ECOC2020, Tu1D.5 (2020).
[8] F. Pittalà, et al., in Proc. ECOC2021, Th2C1.1 (2021).
[9] G. Raybon, et al., in Proc. IEE Photon. Conf., 663-664 (2015).
[10] X. Chen, et al., in Proc. OFC2018, Th4C.1 (2018).
[11] T. Kobayashi, et al., in Proc, OFC2019, Th4B.2 (2019).
[12] M. Nakamura, et al., in Proc. ECOC2019, Tu.2.D.5 (2019).
[13] X. Chen, et al., et al., in Proc. OFC2021, F3C.5 (2021).
[14] P. W. Berenguer, et al., J. Lightwave Technol. 34(8), 1739 - 1745 (2016).
[15] J. J. Shynk, et al., in Proc. IEEE Signal Process Mag, 9(1), 14-37 (1992).
[16] T. Pfau, et al., J. Lightwave Technol. 27(8), 989-999 (2009).
[17] J. Cho, et al., in Proc. ECOC2017, M.2.D.2 (2017).
[18] G. Böcherer, et al., IEEE Trans. Commun., 63, (12), 4651-4665 (2015).
[19] M. Nakamura, et al., in Proc. ECOC2018, We3G.5 (2018).